Journal of The Electrochemical Society, 2021 **168** 024506

Multiple Reaction Pathways for the Oxygen Evolution Reaction May Contribute to IrO_2 (110)'s High Activity

Mai-Anh Ha[1] and **Ross E. Larsen**[1,2,z]

[1]*Computational Science Center, National Renewable Energy Laboratory, Golden, Colorado 80401, United States of America*
[2]*Renewable and Sustainable Energy Institute, University of Colorado Boulder, Boulder, Colorado 80309, United States of America*

Density functional theory calculations in conjunction with statistical mechanical arguments are performed on the rutile IrO_2 (110) facet in order to characterize multiple reaction pathways on the surface at the highest active limit (the stoichiometric surface with all metal sites available) and at the lowest active limit (the oxygen-terminated surface). Alternative pathways to the oxygen evolution reaction (OER) are found, with multiple pathways determined at each step of the four proton-coupled electron transfer reaction. Of particular interest is the detailed characterization of a co-adsorption pathway utilizing neighboring, adsorbed O, OH species in order to evolve oxygen; activation energies of this pathway are <0.5 eV and therefore easily surmountable at the high operating potentials of OER. We also determined that surface Ir atoms can potentially participate in deprotonating an OOH* intermediate; the activation energy to this is 0.67 eV on the oxygen-terminated surface. These theoretical findings explain in part the high activity present in iridium oxide catalysts and also provide insight into the mechanistic pathways available on metal oxide catalysts, which may require the concerted interaction of nearest neighbor co-adsorbates to produce chemicals of interest.

 [DOI: 10.1149/1945-7111/abdeea]

Manuscript submitted October 10, 2020; revised manuscript received December 22, 2020. Published February 5, 2021.

Supplementary material for this article is available online

Hydrogen (H_2) exists an important chemical commodity, both as a precursor to reactions as diverse as Fischer-Tropsch synthesis and the Sabatier reaction for desirable hydrocarbons; the Haber-Bosch process for ammonia generation; and as a source for power in gas turbines and fuel cell vehicles.[1–3] However, the majority of hydrogen is produced via the cheaper process of steam methane reforming (SMR), which requires the use of fossil fuels and high–temperature (700°C-1000°C) conditions.[4] In contrast, the electrolysis of water to produce hydrogen and oxygen remains an attractive, clean alternative and operates under ambient conditions; coupling this process to intermittent, renewable sources of energy such as solar and wind may drive down the cost of electricity to run the electrolyzers, but the use of platinum group metals (PGM) in the catalyst and component coatings keeps cost significantly higher than SMR.[5]

In particular, for the reactions at work in water electrolysis, the oxygen evolution reaction (OER) requires the most PGM catalyst and OER occurs five to six orders of magnitude slower than the hydrogen evolution reaction (HER).[5] Iridium/iridium oxide (Ir/Ir–O) catalysts remain the standard, maintaining high activity and durability under the high potentials and extreme pH conditions typical of electrolysis.[6,7] For electrolysis to become cost-competitive, reduced-PGM or non-PGM materials must be used. Iridium-based catalysts have been studied in various ways: theoretically, in the context of a volcano plot[8,9]; *in-situ* studies to track changes in iridium's oxidation states[10–14]; and assessed from half-cell to single-cell testing, for improved activity and durability performance.[15–17] Theoretical studies of Ir activity are complicated by the well-known fact that at the sustained, high potentials of OER, Ir-based catalysts oxidize and often contain the rutile phase with various percentages of facet families.[15,18–20] Pavlovic et al. observed at potentials >1.2 V, Raman spectra of their hydrous iridium oxide samples begin to display peaks for the E_g (550 cm^{-1}) and B_{2g} modes (720 cm^{-1}) specific to rutile iridium oxide; by 1.8 V, these peaks are strong and sharp. Since the lifetime of commercial proton exchange membrane electrolyzers is typically ~5 years, operating at 1.8–2.0 V, some rutile iridium oxide is most likely present in the catalyst[20] so more complex views of what the active materials and facets are in the catalysts need to be considered.

Often, mechanistic insights from theoretical calculations are limited to one pathway[8,21] which may provide a limited assessment of catalytic activity for more complicated forms of the catalyst. Recently, a number of studies have linked macroscopic properties to the *ensemble* of inter-facial structures at the interface: in clusters, thermally accessible isomers contribute to high activity and resistance to sintering[22–24]; at the surface, the interface can accommodate a range of facets[15,25] or mixed-compositions,[15,16,26,27] which lead to desirable products. Likewise, the ensemble of reactive intermediates at the interface may more accurately represent catalytic activity by introducing multiple pathways to a product; studying the (110) rutile iridium oxide (IrO_2) for the oxygen evolution reaction is a model case of a well-known material and thermodynamically stable facet.[28] In addition, considering the ensemble of intermediates can provide significant mechanistic insights to reactions on metal oxides and enhance our knowledge of multi-step, electrochemical reactions.

In this theoretical study, we focused on characterizing multiple OER pathways on the (110) facet, finding numerous possible pathways on the stoichiometric surface; then, we evaluated the viability of these pathways on the oxygen-terminated surface that is expected to form under the potentials needed to achieve OER. The stoichiometric surface represented the high activity limit, where all surface metal sites are available; the oxygen-terminated surface represented the low activity limit, where all surface metal sites are covered in oxygen except for a single active site. As noted in many studies, at high potentials, iridium oxide is oxygen-terminated and may accommodate a range of O/OH coverages.[9,10,29] Density functional theory calculations are performed in conjunction with statistical mechanical arguments: many isomers may be thermally accessible at room temperature, of particular interest are isomers in which spontaneous dissociation of molecular intermediates occurs, resulting in co-adsorbed species and leading to alternative mechanisms to OER; once these isomers of interest are identified, climbing image nudged elastic band calculations (cNEB)[30–33] are performed to find reaction barriers to assess the minimum energy pathway and determine the activation energy at various steps of the OER.

[z]E-mail: Ross.Larsen@nrel.gov

Methods

The Vienna Ab-Initio Simulation Package (VASP 5.4)[34–37] with the most recent projector augmented wave (PAW)[38,39] pseudopotentials was utilized to calculate all plane-wave density functional theory calculations. We employed the PBEsol[40] exchange-correlation functional, a version of the Perdew–Burke–Ernzerhof (PBE)[41] functional revised for solids and known to reproduce well iridium oxide's crystal field splitting as observed in X-ray photoelectron spectrocopy.[42] The bulk unit cell was evaluated with an expanded basis set of 520 eV and dense Monkhorst-Pack grid of $8 \times 8 \times 8$. The unit cell's lattice constant optimized to a slight increase of 0.3% from experiment; the unit cell was then sliced, exposing the (110) facet and grown to (2×4) slab with a depth of four trilayers.[43] Full view of the surface may be seen in SI Fig. 1 (available online at stacks.iop.org/JES/168/024506/mmedia); labels are overlaid on the surface identifying differences between the (1×1), (1×2), and (2×4) surfaces. The Monkhorst-Pack grid for these respective surfaces were $5 \times 5 \times 1$ for (1×2); $3 \times 6 \times 1$ for a (2×2) and $1 \times 1 \times 1$ for (2×4) with shifts in the x- and y-direction, resulting in a slightly more stable surface. A vacuum gap of >13 Å was used in order to avoid spurious interactions between periodic images. Strict convergence criteria of 10^{-6} (10^{-5}) eV were applied to electronic (geometric) relaxations; the kinetic energy cut off of the plane waves basis sets were expanded to 400 eV.

Adsorption energies were determined via the relation $E_{ads} = E_{surf+ads} - E_{surf} - E_{gas,ads}$, where $E_{surf+ads}$ was the total energy of the surface with adsorbate, E_{surf} was the total energy of the clean surface without adsorbate, and $E_{gas,ads}$ was the total energy of the gas phase adsorbate (H_2O, OH, O, OOH, O_2). We note that reference energies of gas phase adsorbates were calculated appropriately utilizing the PBE functional, instead of the solid-state variant, PBEsol. In our search of local minima at each step of the OER reaction, we adsorbed key reaction intermediates at atomic, bridging, and hollow sites; rotated every 45 degrees; and in different configurations (bent, straight, and flipped in various ways to enable unique coordination of intermediates to the surface atoms). In our minima search for these adsorbed species, we found many unique configurations. This allowed us to incorporate statistical analysis of these species by evaluating the Boltzmann probability (P_i) by taking the Boltzmann distribution of each identified intermediate (e^{-E_i/k_BT}) divided by the sum of the distributions of all relevant minima:

$$P_i = \frac{e^{-E_i/k_BT}}{\sum e^{-E_i/k_BT}},$$

where E_i is the ith energy of a local minimum for the adsorbed species, k_B is the Boltzmann constant, and T is the temperature, taken to be 300 K throughout. This provides an assessment for what isomers beyond the lowest energy one would be thermally accessible to the system at 300 K.

The formation energy of open metal sites on the otherwise fully oxygen-terminated surface was evaluated similarly to the formation energy of vacancies on the stoichiometric surface.[44] The formation energy for a single open site (V_O) is as follows: $E_{form}(V_O) = E_{tot}$ (with open site)—E_{tot}(no open sites) + ½ $E_{gas}(O_2)$, where E_{tot} (with open site) is the total energy of the surface with the open site, E_{tot} (no open sites) is the total energy of the oxygen-terminated surface with no open sites, and $E_{gas}(O_2)$ is the total energy of the gas phase O_2 molecule. Likewise, the formation energy for two open sites (V_{2O}) is as follows: $E_{form}(V_{2O}) = E_{tot}$ (with two open sites)—E_{tot} (no open sites) + $E_{gas}(O_2)$.

Climbing image nudged elastic band calculations were performed to determine the barriers to minimum energy pathways, initial and final states utilized the isomers found during our local minima search.[31,32,45,46] Post-processing of isomers was performed, extracting electronic information for bonding analysis such as charge-transfer via the Bader charge algorithm and orbital overlap from projected density of states.[47–51]

Results and Discussion

Discussion of this paper's results is divided into two sections, highlighting the available isomers of adsorbed species at the iridium oxide interface and comparing the stoichiometric surface to the oxidized surface. In the first section, the **Limit of High Activity, All Surface Ir Sites Available: Stoichiometric Surface,** all the unique isomers of adsorbed species found during our minima search are presented in the context of the 4-step proton-coupled electron transfer mechanism. This enabled us to map out different pathways at potentially rate-determining steps such as the deprotonation of OH* to O* + H* and evolving oxygen via co-adsorption (O* + OH*) and the typical OOH* pathway; knowing these pathways, we were then able to calculate mechanistic barriers (activation energy, E_A). In the second section, **At Higher Potentials, Lower Limit of Activity: O-terminated Surface**, we evaluate the relevant pathways found in the first section in the context of an oxidized surface. In order to further delve into the possibility of multiple open, active sites forming as oxygen is evolved from the oxidized surface, ab-initio calculations were performed removing a single oxygen from the O-terminated surface (one open site) as compared to two oxygens from the O-terminated surface (two open sites). Mechanistic barriers are also calculated for the pathways found in the first section on the oxidized surface. The formation energies of open sites and activation energies of various pathways provide a detailed assessment of the viability of different mechanisms to OER on the oxidized surface.

Limit of high activity, all surface Ir sites available: stoichiometric surface.—The generally accepted mechanism for OER in this system involves adsorption of water onto the surface (H_2O*, with the * denoting adsorption), followed by sequential reactions producing four intermediates (OH*, O*, OOH*, O_2*) prior to desorption of O_2.[8,9] This is often presented as a stepwise reaction profile, in which an ideal catalyst would have a free energy barrier of 1.23 eV at each step, corresponding to the thermodynamic redox potential of 1.23 V for oxygen evolution. However, the complexity of electrochemical reactions is such that many approximations must be made that are non-trivial to compute, in order to capture the solvation and potential gradient.[9,52,53] Typically, a small surface is studied of (1×2) in order to look at OER or incorporate non-trivial effects of water and pH, but the interactions of OER reaction intermediates may be sensitive to adsorbate spacing so here we expand the size of the surface to reduce this effect.[8,9,54,55] We note that a (1×2) surface exposes only 2 metal surface sites with surface dimensions of 6.37 Å × 6.30 Å; this limits the sampling of configurations of adsorbates considerably. We visualize this in comparison to our surface in SI Fig. 1b; moreover, we tally the available sites on the surface in SI Table I. Our (2×4) quadruples the number of available sites for support-adsorbate interactions; our surface dimensions are 12.74 Å × 12.60 Å. In this paper, we focus on the computationally intensive mapping of reaction pathways on a large (2×4) surface; the high reactivity of iridium oxide resulted in the discovery of many catalytically relevant isomers.

In our search for the local minima at each step, we found that key reaction intermediates can bind to unique adsorption sites and spontaneously dissociate to become a mix of co-adsorbates. Thus, our reaction scheme for all of these adsorbed intermediates is illustrated schematically in Scheme 1 with brackets [ ] to suggest the ensemble of intermediates present at each step of the OER. We summarize briefly in Table I the total number of unique isomers found at each OER step and categorize the isomers by their adsorbed species. By "isomer" we mean any set of adsorbates having the same stoichiometry so, for example, co-adsorbed (O_2*, H*) and a single OOH* are considered isomers in our discussion. We stress that many unique minima were found in our minima search and these are displayed in the Supporting Information (SI). For brevity, in Fig. 1, we visualize only the four lowest minima of the first three steps of OER. In Scheme 2 and Fig. 2, we discuss and display catalytically

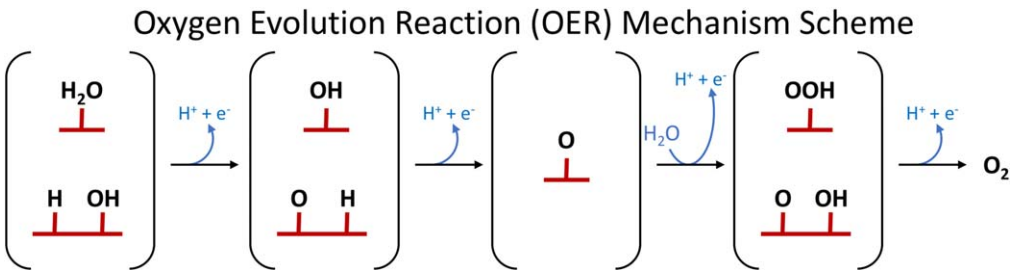

Scheme 1. Schematic describing the oxygen evolution reaction (OER) mechanism. At each reaction step, an ensemble of isomers, including co-adsorbates, is present and defined by a bracketing of [ ] adsorbed species in our diagram, resulting in alternative pathways that can occur on the surface e.g. OH* → O* + H*, where * denotes an adsorbed species. The solvent-mediated mechanism of the proton-electron transfer of $H^+ + e^-$ is approximated to a reference energy of ½ H_2 in the computational standard hydrogen electrode (SHE).[8]

Table I. Summary of unique isomers found at each step of the OER mechanism on bare IrO_2.

OER Step	# of Isomers Found	Summary
[H_2O*, H* + OH*]	7	Isomers I-III: H* + OH* Isomers IV-VII: H_2O*
[OH*, O* + H*]	7	Isomers I-III, V-VII: OH* Isomer IV: O* + H*
[O*]	4	Unique Adsorption Sites
[OOH*, O* + OH*]	16	Isomers I-V, VIII-IX, XIV: O* + OH* Isomer VI: O* + O* + H* Isomer VII, X-XI, XV: OO* + H* Isomer XII-XIII: OOH* Isomer XVI: O_2 + H*

relevant isomers for the fourth and most complex step of OER. As noted in Table I, 16 unique isomers of OOH*, OO* + H*, O* + OH*, and O* + O* + H* may contribute to this OER step. In all figures showing energies of different isomers, the adsorption energy of the total isomer is given as $E_{adsorbate}$ and the energy of higher-lying isomers is given as the *difference,* $\Delta E_{adsorbate}$, from the lowest isomer energy. The isomers are numbered by roman numerals in order of lowest to highest energy (i.e., most to least strongly adsorbed).

In this study, we focus on adsorption energies and reaction enthalpies of the OER. While most theoretical studies utilize the free energies, each theoretical study may draw upon different reference calculations (e.g. the use of more accurate, localized basis sets in programs such as Jaguar), utilize NIST tables, or extract an energy correction from experimental data or previous base-lining theoretical work.[9,55,56] In general, the relative differences in energy between reaction steps of adsorbed species are less at room temperature than the energy differences reported here, when including vibrational contributions to the zero point energy and the entropy. Likewise, the trends observed in adsorption energy will also typically correspond to adsorption free energies at moderate temperatures of ~300 K.[57] We attempt to consider thermal effects by utilizing statistical mechanical arguments related to the Boltzmann populations of various isomers at the room temperature of 300 K: Fig. 1 highlights nearly degenerate isomers of the [H_2O*, OH* +H*], [OH*, O* + H*] reaction intermediates and their respective Boltzmann populations.

This a simplifying approximation, which does not include the stability and dynamics of hydrogen-bonding networks of the solvent, the potential gradient, or the possible chemical-Coulombic effects of electrolyte ions. However, the incorporation of these effects across dozens of isomers is non-trivial to compute. We anticipate, however, that the mechanistic pathways illustrated in this study will give some measure of insight into the OER; incorporation of more realistic, in situ conditions is the focus of future work. The considerable number of isomers at each reaction step of OER detailed here outline the various pathways to OER and point toward mechanisms that may be far more complicated than a single pathway: the inclusion of experimental conditions will most likely further add complexity to the pathways possible, meriting a separate study. Moreover, we expect the effect of vibrational contributions to be considerably greater at varying temperatures and pressures present in experiments such as temperature programmed desorption/reaction and in situ X-ray photoelectron spectroscopy.

For the first step, we show that H_2O dissociates upon adsorption on IrO_2 and that there is no barrier to this dissociation, thus confirming that IrO_2 (110) is highly active for splitting water at the surface. In general, the undercoordinated Ir_{5f} sites are the preferred adsorption sites of O-containing species; in other rutile (110) surfaces, these are also the catalytically active sites for water dissociation.[28,54] Of the isomers found, the three lowest isomers, composing 99.99% of the Boltzmann population at room temperature, are of the dissociated water. The dissociated OH* and H* are further stabilized due to hydrogen-bonding of ~1.8–2.7 Å to surface (O_s) and bridging oxygens (O_b) on the stoichiometric surface, as can be seen in Fig. 1a.

In the next step to OER, we encounter the first possible rate determining step i.e. deprotonation of OH* to form neighboring O* and H* adsorbates. We identified multiple hydroxide adsorption motifs: the three lowest energy motifs of OH* account for 99.96% of the Boltzmann populations at room temperature and feature hydroxide adsorbed onto an Ir_{5f} atom with hydrogen bonding of 2.1–2.7 Å to bridging and surface oxygens. The isomers differ only in the orientation of the OH bond, as shown for the three images in Fig. 1b. The fourth isomer is a dissociated OH pair with a hydrogen bond of 1.9 Å between O* and H*; while this higher energy isomer only represents 0.04% of the Boltzmann population at room temperature, it is possible that this isomer may be further stabilized at high potentials or due to hydrogen bonding with the electrolyte. We computed the activation energy using the cNEB method for the isomers I-III dissociating to form co-adsorbed O* and H* and provide the interpolated images between the reactant and product configurations in SI Figs. 5–7. We found that for OH dissociation on this surface, isomers II and III rotate to become isomer I before the

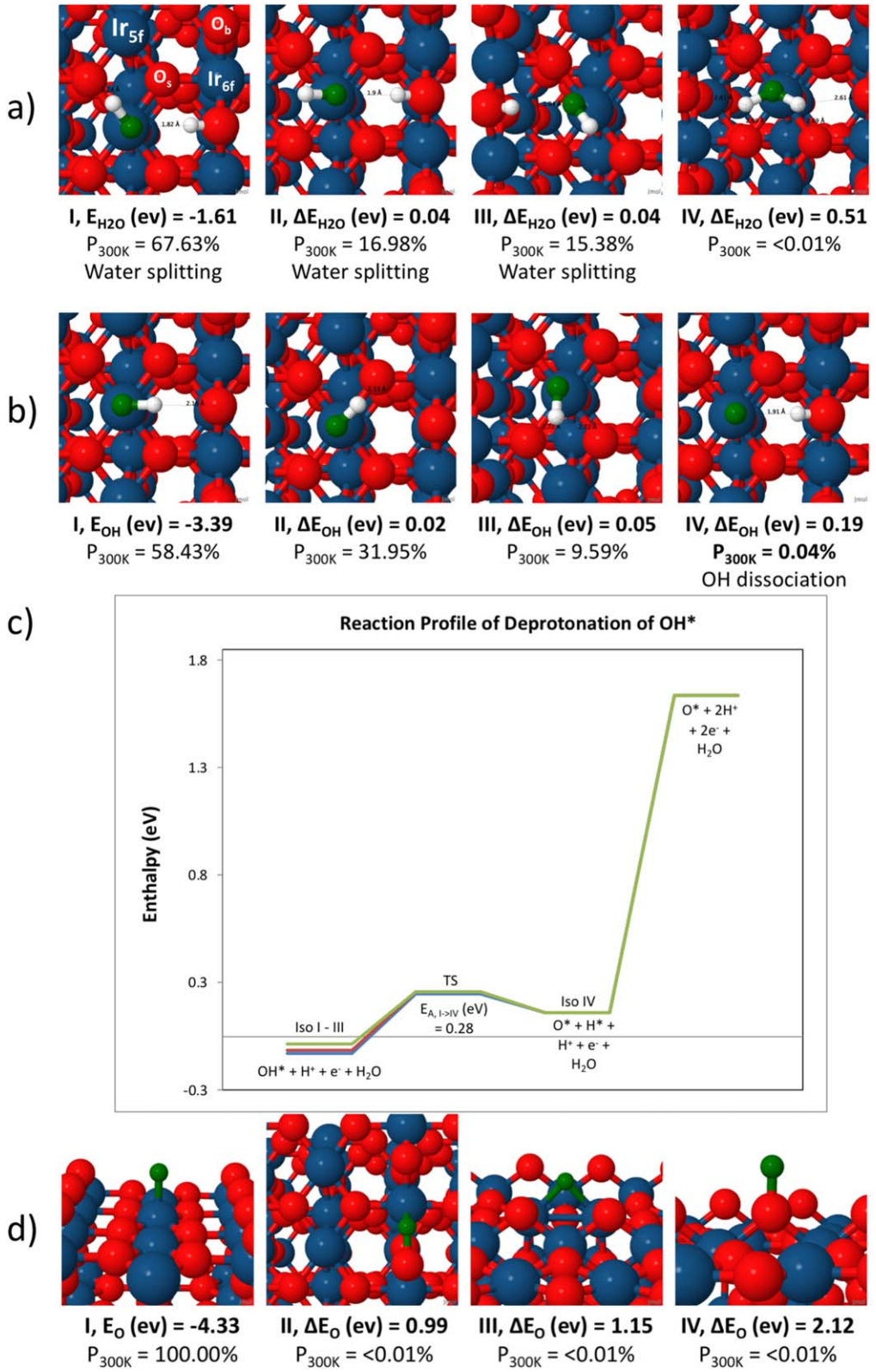

Figure 1. Lowest four minima of adsorbed (a) **H_2O*, OH* + H* species**; (b) **OH*, O* + H* species**; (d) **O* species** on the rutile IrO_2 (110) surface with adsorbed energy of the global minimum structure (E_{ads}), relative energies of local minima with respect to the global minimum structure (ΔE_{ads}), and Boltzmann populations at 300 K (P_{300K}). (c) **Reaction Profile of OH* → O* + H*** in the context of the 4-step OER visualized. On (a) Labels on the surface iridium oxide's atoms are provided: Ir_{5f} indicates a surface 5-fold coordinated iridium atom, Ir_{6f} is a surface 6-fold coordinated iridium atom, O_s is a surface oxygen (coordinated to one Ir_{6f}, two Ir_{5f}), O_b is a bridging surface oxygen (coordinated to two Ir_{6f}). Iridium atoms are in teal, oxygen atoms belonging to the surface are in red, oxygen atoms belonging to the adsorbed species are in green, and hydrogen atoms are in white. * refers to an adsorbed species. Activation energy (E_A) denotes the transition state energy relative to the initial minimum from calculations utilizing the cNEB method.

Table II. Reaction pathways to OH splitting: OH* → O* + H*.

Reaction Pathways	E_A (ev) (TS)	Summary
I → IV	0.28	Main Pathway
II → IV	0.27	Iso II → (rotate 52.5°) → Iso I → IV
III → IV	0.24	Iso III → (rotate 93.6°) → Iso I → IV

deprotonation can occur. This rotation is barrierless and can be seen as energetically downhill in the reaction coordinates in the SI, indicating that interconversions among isomers I-III should be thought of as continuous rotational motions with a tendency to be in the I orientation rather than as discrete transitions among several minima. In isomers II and III, the long-range hydrogen bonds of 2.7 Å to surface oxygen are now replaced with a stronger hydrogen-bond of ∼2 Å to a bridging oxygen. The rotation is favorable by 0.02–0.05 eV and enables the lowest energy pathways for deprotonation to all pass through isomer I. We summarize the transition states i.e. the reaction barriers in Table II and visualize the reaction profile in the context of OER in Fig. 1c.

We note in Fig. 1c that the third OER step of O* + H* → O* + H may be high in vacuum, but that this barrier may be more easily surmountable in the electrolyte and at the high potentials typical for OER. Due to the non-trivial nature of modeling the proton-electron transfer in a redox reaction, the computational standard hydrogen electrode equates the proton-electron to ½ H_2.[8] This approximation for vacuum calculations contributes to a high energetic barrier. Typically, the Grotthuss mechanism of proton hopping in water may be at most 0.09–0.13 eV; at the equilibrium distance of 2.39 Å between O–O in water, proton hopping is barrierless.[58] Sanchez et al. observed in their in situ X-ray photoelectron studies observed during potentials typical of OER that the ratio of hydroxyl species to oxide species to reduce from 1:2 to 1:3.[14] The Ir 4f signal did not change, suggesting that surface hydroxides desorbed hydrogen to become surface oxide species. Pavlovic et al. specified that below 0.5 V, the Ir 4f spectra remained the same during the applied potential, but that the O 1s spectra showed a majority of O present as OH; above 0.5 V, the O 1s shifted to chemisorbed or oxidic O typical of IrO_2.

In Fig. 1d, we detail the possible adsorption sites for the oxide species, O*. The adsorption site to Ir_{5f} is overwhelmingly preferred; other sites are considerably higher in energy with adsorption sites decreasing in stability from atomic on Ir_{5f} > bridging to Ir_{6f} and O_b > bridging to two Ir_{5f} > atomic on O_b > atomic on Ir_{6f}. Indeed, the adsorption of O* and OH* on a bridging oxygen, such as O*-O_b (Isomers II, IV, Fig. 1), forming an OO* complex, and O_b-OH* (Isomers V-VI, SI Fig. 3), forming an OOH* complex, often occurs on higher energy isomers of from the global minimum. We note that while these may be a higher energy minimum, this may also be an alternative avenue for O_2 evolution subsidiary to more prominent mechanisms such as those described in the next paragraph. In other, less catalytically active metal oxides such as titania, vacancy sites result in greater activity for both the hydrogen evolution and oxygen evolution reactions.[57]

Iridium oxide can exist in some ratio of amorphous to crystalline phases, leading to unique electrochromic features and introducing a considerable number of defect sites due to the non-stoichiometric nature of these surfaces.[59] Indeed, the introduction of an oxygen vacancy may be potentially advantageous to catalysis: an oxygen vacancy will result in the localization of two electrons on Ir atoms to form Ir^{3+}, a species that can be highly active and display electrochromic transitions.[18,59] The mechanistic pathways of forming an oxygen vacancy is beyond the scope of this current study, but we expect that a number of the species found in our minima search (O*–O_b of Isomers II, IV, Fig. 1; O_b–OH* of Isomers V-VI, SI Fig. 3) to contribute to defect formation. We note that a number of studies have probed the electronic localization of Ti^{3+} species due to an oxygen vacancy: the permutations of the two localized electrons in both rutile and anatase are numerous and experimental studies will often detect different states depending on the microscopy technique used.[60–63] We expect rutile iridium oxide to be equally complex.

Following the deprotonation of OH* to O*, water presumably interacts with O* to form the OOH* complex and desorb H: (O* + H_2O → OOH* + H). The dehydrogenation of OOH* to form OO* and H* has been posited as the rate limiting step in OER. Previous studies focused on OOH* oriented with the H pointed into vacuum in order to examine on a geometry that would facilitate OOH* interacting with water (see **Isomer XIII** in Fig. 2).[8,9] In our calculations, we adsorbed OOH* in various configurations (∼200 initial geometries on atomic, bridging, and hollow sites), finding that, at least in vacuum, OOH* is unstable, preferring to fall apart to form isomers of OH* and O* on this surface under these conditions. We note that in previous theoretical studies, their (1 × 2) surface is a quarter the size of our surface and exposes only two active Ir_{5f} sites.[8,9,55] Due to the small size of their surface cell, there may have been interaction between periodic images, preventing adsorbed OOH* from dissociating or binding in various configurations. Moreover, the dimensions of a (1 × 2) surface is only circa 6 Å × 6 Å; in contrast, our (2 × 4) surface is circa 12 Å × 12 Å, allowing us to sample hundreds of initial geometries. At room temperature, the Boltzmann populations of O* and OH* (isomers I-V) total to 100% (see SI Fig. 8 for visualization of all isomers). However, it is worthwhile to consider higher energy isomers since under operating conditions there may be additional stability provided by solvation and the operating potentials of OER. With these considerations in mind, the last step of OER is examined assuming it may proceed along two different, unique pathways: the OOH* pathway or the co-adsorption pathway utilizing O* and OH* in close proximity to each other. In Scheme 2, we provide a schematic of these two pathways.

In Fig. 2, we visualize the relevant isomers to these two pathways. Some isomers of co-adsorbed O* and OH* were >4 Å apart and therefore catalytically inert; some isomers featured OH* and O*–O_b, these may be found in the SI. Stoichiometrically, the OOH* and co-adsorption pathways are the same, but the reaction between OH* and O* co-adsorbates is energetically much more favorable in vacuum than when OOH* remains intact. The most commonly studied OOH* configuration, isomer XIII, is calculated to lie 2.01 eV higher in energy than the co-adsorbed O*/OH*, isomer I. Moreover, there is no barrier to the deprotonation of isomer XIII: this spontaneously occurs, with H* preferring to adsorb to the bridging oxygen in isomers X and XI. Gauthier et al. also reported this in their solvation studies on rutile iridium oxide, where they pointed out that in order to observe OOH* interactions with explicit waters, they had to constrain the H to prevent spontaneous dissociation to a bridging oxygen or a terminated oxygen on Ir_{5f}.[9]

It is possible that the OOH* moiety could be stabilized in the presence of an electrolyte, making this path the preferred one, thus, we calculated the activation energy to deprotonation of an intact OOH* moiety (isomer XII → isomer XV). In vacuum, the transition state requires 0.76 eV to occur (the full reaction coordinate is visualized in SI Fig. 13). This mechanism is a unique OOH* pathway that to our knowledge has not been characterized before: on the stochiometric IrO_2 surface the OOH* is deprotonated by a surface Ir atom instead of a bridging oxygen. Moreover, in the initial state the O–O bond in the OOH* is ∼1.4 Å; in the final deprotonated state, the O_2* complex is 1.28 Å and fairly close to the bond length

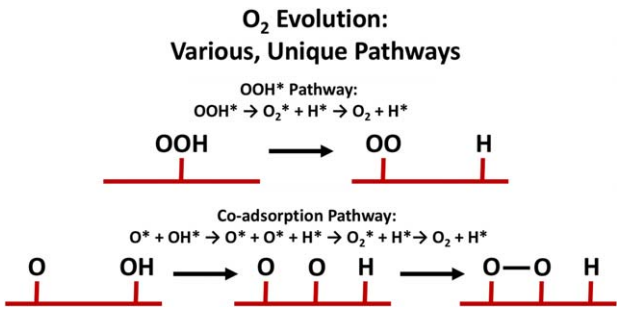

Scheme 2. Schematic describing alternative pathways to O_2 evolution via a single adsorbed OOH* pathway or co-adsorbed O* + OH* pathway. * refers to an adsorbed species.

of ∼1.2 Å of gaseous O_2. We note that the desorption of different O_2* complexes (isomers X, XII, and XV) will have high energetic barriers in vacuum, but that these barriers may be more easily surmountable in situ with solvation and the applied potential of an electrochemical cell.

In contrast to the direct OOH* pathway, the co-adsorption pathway requires two nearest-neighbor adsorbates O* and OH* to occur. The two-step process for the co-adsorption pathway involves deprotonation of an OH* → O* + H*, followed by formation of the OO* species with a nearby H*. We identified three, nearest-neighbor O* and OH* isomers (see Fig. 2): I, IV, and V, with the lowest energy isomer I being much more stable than the others, accounting for 98.3% of the population by Boltzmann weighting. The addition of a nearest neighbor O* next to OH* resulted in OH* hydrogen bonding to that O* (∼2.0 Å) instead of the bridging oxygen;

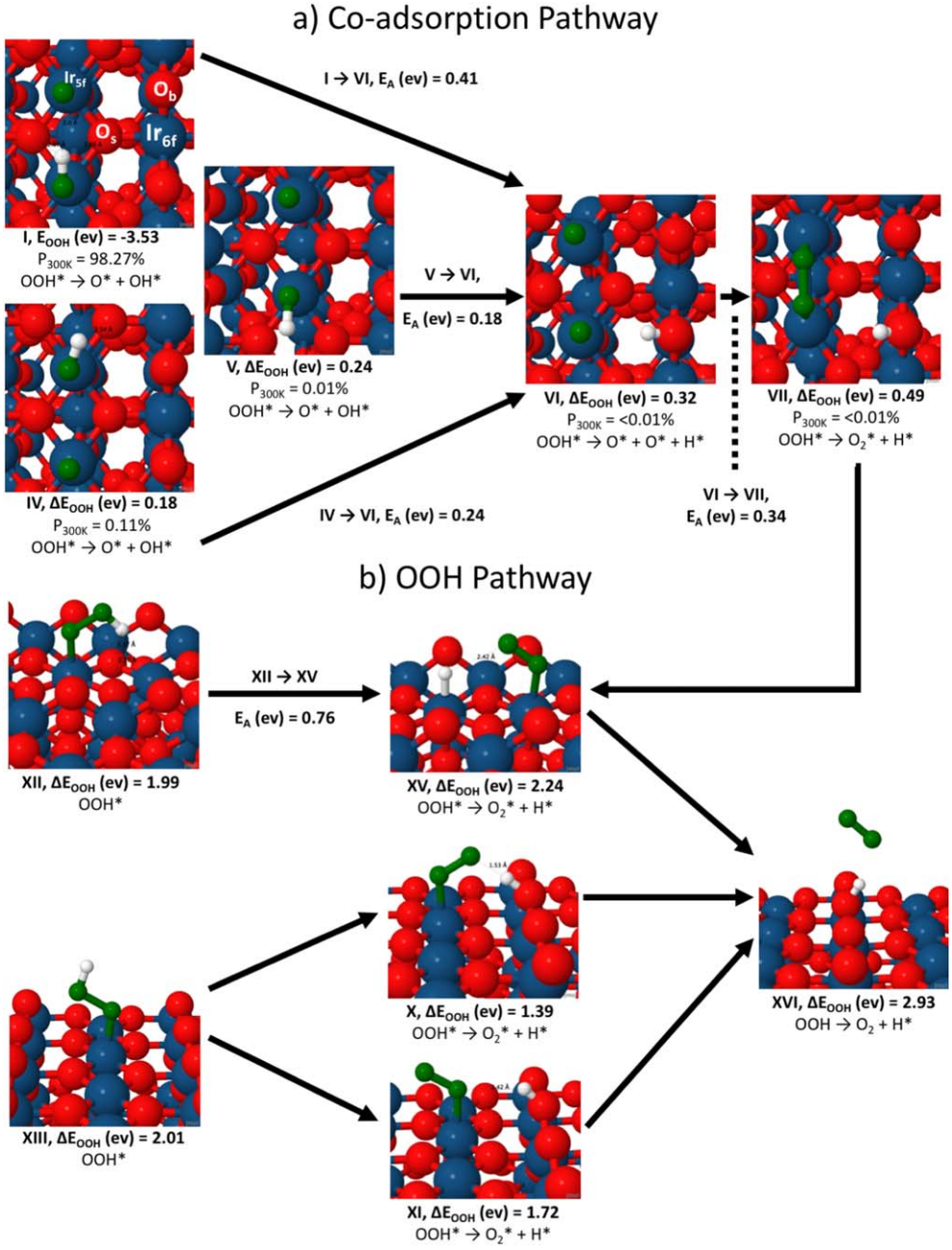

Figure 2. (a) The **co-adsorption pathway** is detailed with relevant isomers that would contribute to the pathway of **O* + OH* → O* + O* + H* → O_2* + H***. (b) The **OOH pathway** is detailed with relevant isomers that would contribute to the pathway of **OOH* → O_2* + H* → O_2 (desorbed) + H***. The adsorption energy E_{OOH} is denoted for the global minimum (isomer I), but all other isomers display the energy relative to the global minimum (ΔE_{OOH}). Boltzmann populations at the room temperature of 300 K are listed underneath the isomer. * refers to an adsorbed species. In the Supporting Information, full reaction coordinates are visualized in SI Figs. 9–13. Activation energy (E_A) denotes transition state calculations utilizing the cNEB method.

moreover, there may also be additional stabilization due to hydrogen bonding to surface oxygen ~2.7 Å. Deprotonation of isomer I requires a higher activation energy of 0.41 eV due to strong hydrogen bonding between the neighboring O* and OH*. In contrast, isomers IV and V feature OH* coordinated to surface oxygens (diffuse hydrogen bonding of ~2.5–2.7 Å); likewise, their activation energies to deprotonation are lowered to 0.24 and 0.18, respectively. The full sets of energy as a function of reaction coordinate may be found in SI Figs. 9–11. The higher energy isomer, VI, represents the deprotonated product O* + O* + H*; isomer VII, corresponds to the final O_2* + H* product.

Following the formation of co-adsorbed O* + O* + H* (isomer VI), the formation of O_2* + H* (isomer VII) results in a barrier of 0.34 eV to distort the two Ir–O bonds to allow formation of an O_2* molecule bridging the two iridium atoms (the full reaction coordinate is visualized in SI Fig. 12). We note that our reaction coordinate followed the isomer VI through two transition states: the first through the hydrogen bond breaking and reforming again to isomer VI; the second to OO* formation. Breaking the hydrogen-bond was comparable in magnitude to our discussion surrounding isomers of OH*, thus we focus our discussion here on the formation of the O_2* complex. This O_2* complex features a bond length of 1.41 Å and we hypothesize that this complex bound to two iridium atoms most likely interconverts into either an O_2* bound to one iridium atom (isomers X, XI, and XV) or may be re-protonated into an OOH* complex (isomers XII and XIII) in low pH conditions. As noted earlier in the paper, we anticipate that deprotonation will be strongly pH and electrolyte dependent, because the presence of water and ions (protons or hydroxide) could allow hydrogen bonding to take place continuously throughout the reaction. However, these calculations highlight that the formation of O_2* may potentially bypass the typically suggested mechanism of water interacting with an adsorbed O* to form an OOH* complex.

In Fig. 3, we summarize the full reaction profile for the OER mechanism on stochiometric rutile IrO_2 (110) **(TOP)** and contextualize the co-adsorption pathway **(MIDDLE)** and OOH* pathway **(BOTTOM)** within the energies of the overall mechanism. It becomes readily apparent that the OER mechanism on iridium oxide is not a simple stepwise reaction profile through a single path; various isomers are thermally accessible at each step for adsorbed [H_2O]*, [OH]*, and [OOH*] species. In particular, we highlight that the formation of O_2 may pass through either the co-adsorption pathway (e.g. initial states of isomers I, IV, and V) or the OOH* (e.g. initial states of isomer X's OO*, isomer XII's OOH*) pathway. Although the OER mechanism in past studies focused on isomer XIII, the large energy of isomer XIII suggests that various alternative pathways that exploit the high reactivity of surface Ir_{5f} atoms also merit consideration. Co-adsorbed O* and O* species on surface Ir_{5f} are ~3 Å apart; therefore, the co-adsorption pathway requires only 0.34 eV to bend the two Ir–O* bonds ~0.6 Å towards each other in order to form the bridging transition state of O–O*. Moreover, surface Ir_{5f} atoms can also deprotonate an OOH* moiety (isomer XII), resulting in an O_2* complex with an O–O bond length of ~1.3 Å (close to gaseous O_2's bond of ~1.2 Å). We note that isomer VII, the bridging OO* complex, may convert to isomer XV by breaking one Ir–O* bond; the large difference in their energies may be due to energy required to break the Ir–O* bond modulated somewhat by the placement of the hydrogen. In this way, the co-adsorption pathway and OOH* pathway can converge and overlap due to the configurations of certain isomers.

For OER in alkaline media, other papers have suggested different mechanisms, often considering OOH* to be a transient species and highlighting the importance of deprotonating OH* to O* in order to form O_2*.[64–66] Recombination of adsorbed species O*/OH* species to form an adsorbed O_2* complex is considered the dominant mechanism on Ni-based and Co-based catalysts.[64–66] In their hybrid quantum-mechanics/molecular mechanics study of cobalt oxide, Wang et al. calculated a 0.10 eV barrier to form a bridging Co–O–O–Co complex; the displacement of that complex and breaking a Co–O bond required an activation of 1.52 eV.[65] In contrast, Ping et al.'s calculations on a (1 × 2) surface of IrO_2 (110) found a 0.62 eV free energy barrier at U = 1.53 eV vs NHE to forming an Ir–O–O–Ir complex.[55] However, on a (1 × 2) surface, where only two Ir_{5f} sites are exposed, they are modeling a surface with a high concentration of OO*. Our (2 × 4) surface of iridium oxide approximates 25% of Ir sites occupied by an OO* bridging complex; due to the periodicity of their cell, their (1 × 2) surface results in 100% of Ir sites occupied by an OO* bridging complex. Therefore, the concentration of exposed surface sites most likely impacts the pathways found here on the bare surface. We discuss the role of this high effective concentration in the following section on the oxygen-terminated surface, where we evaluate the viability of the isomers we found on stoichiometric IrO_2 for the co-adsorption and OOH* pathways on an *oxygen-terminated* surface.

At higher potentials, lower limit of activity: O-terminated Surface.—At the operating potentials of OER, the rutile (110) surface is terminated with some mixture of oxygens and hydroxides and these surface species can influence the stability of key reaction intermediates.[9,10,18,29] Rossmeisl et al. predicted in their theoretical study of rutile oxides (IrO_2, RuO_2, and TiO_2) that at potentials >1.4 V, the O*-covered surface is more stable than the OH*-covered surface.[29] Since typical operating potentials for OER range between 1.8–2.0 V, we chose to focus our study of the mechanistic pathways determined in the previous section on the more stable O*-covered surface.

In the previous section, we introduced the possibility of multiple reaction pathways and in this section we focus our evaluation of two of the pathways on the oxygen-terminated surface: the co-adsorption pathway utilizing neighboring O* and OH* species and the intact OOH* pathway. The viability of these pathways is determined by the formation energies of available metal sites on the surface, e.g., the energy required to remove an oxygen from the surface. The co-adsorption pathway may be classified as a pathway requiring the interaction of adsorbed species on *two* neighboring metal sites (2 M). In contrast, many of the intermediates for the OOH* pathway may be classified as pathways requiring only *one* metal site (1 M). Once surface Ir atoms are oxygen-terminated, the stoichiometries of these pathways now differ due to the total number of atoms in the system not being the same. Thus, to compare the pathways, we denote the key reaction intermediates with the generalized classification of utilizing two metal sites (2 M) or one metal site (1 M). Ostensibly, the co-adsorbed O* and OH* pathway may also occur via one open site, which would be filled an OH*, with the partner O* supplied by an O from the already O-terminated neighbor. The OH* may originate from the favorable water-splitting reaction on the surface, from adsorbing OH^- from an alkaline electrolyte, or from protonation of O_T* in an acidic electrolyte.

In Fig. 4, we highlight some of the possibilities for one and two open sites on the surface. For one open site, the oxygen can be removed from a termination adsorbed on an Ir_{5f} (O_T) or a bridging (O_b) site adsorbed to two Ir_{6f}. For two open sites, there are many possible permutations of open sites; in our search, we found 13 unique configurations and the ranges of energies of these are summarized in Table III (see SI Fig. 14 for more details). Unsurprisingly, the formation energy required for a single oxygen removed from surface Ir_{5f} is considerably lower than that of a bridging oxygen coordinated to two Ir_{6f} (two Ir–O bonds must be broken). Moreover, this trend carries over to the consideration of two

Table III. All possible configurations of 2 open sites, V_{2O}, on an O-terminated IrO_2 (110) surface.

Config.	Sites	$E_{form}(V_{2O})$ (eV)
I–V	2 O_T on Ir_{5f}	1.44–1.54
VI–VIII	O_T on Ir_{5f}, O_b on Ir_{6f}	2.98–3.05
IX–XIII	2 O_b on Ir_{6f}	4.44–4.59

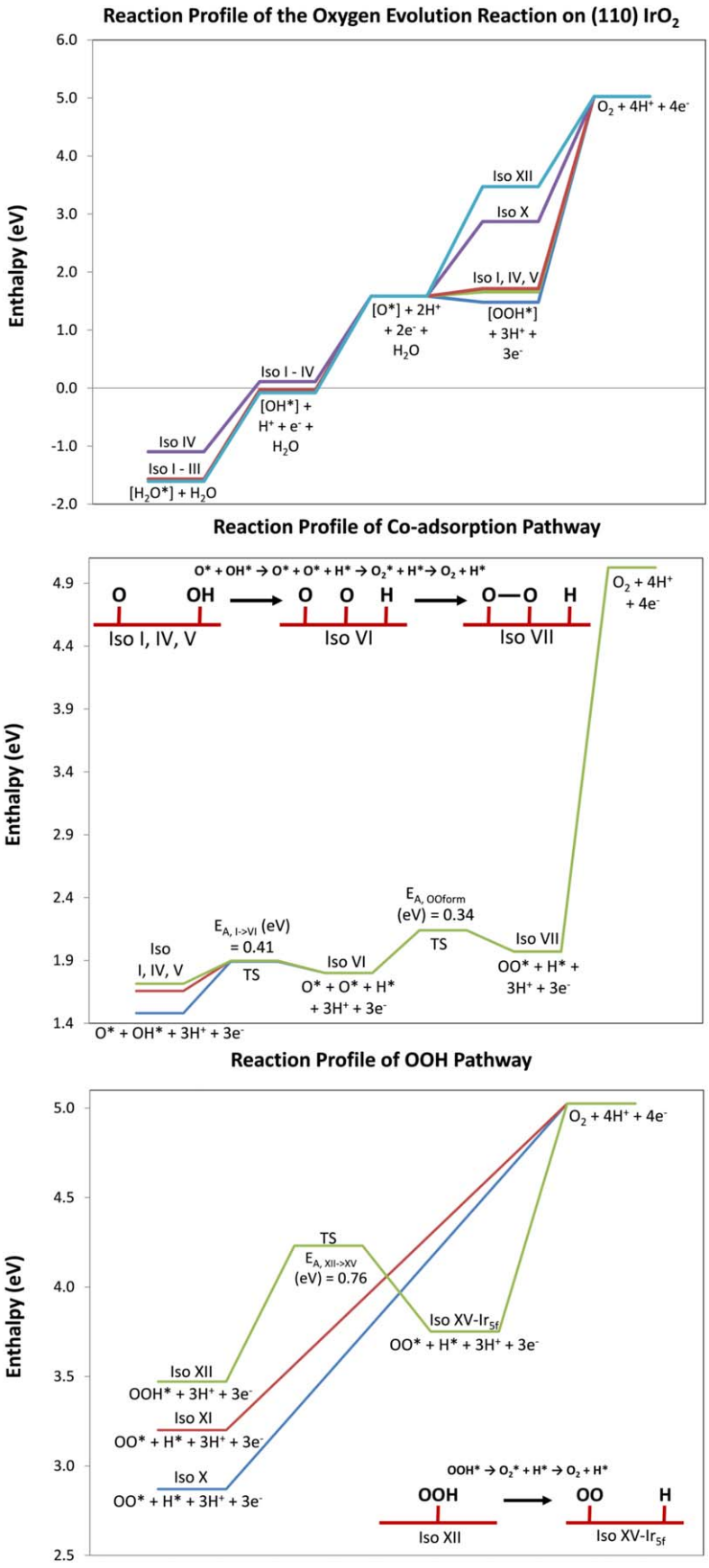

Figure 3. **(TOP)** Full reaction profile of the OER, highlighting relevant isomers that may be initial geometries to a particular OER step. Not all isomers are displayed for brevity. **(MIDDLE)** The co-adsorption pathway for the final reaction step within the energetic context of the full OER mechanism, noting various transition states. **(BOTTOM)** The OOH* pathway for the final reaction step within the energetic context of the full OER mechanism, isomers X-XI feature a deprotonated OO* complex, and isomer XII features an intact OOH*. Activation energy (E_A) denotes transition state (TS) calculations utilizing the cNEB method.

open sites: removing two terminating oxygens on Ir_{5f} requires a formation energy of 1.44–1.54 eV (isomers I-V in Table III, isomer I in Fig. 4), whereas removing a single bridging oxygen and oxygen on Ir_{5f} require a formation energy of 2.98 eV (isomer VI in Fig. 4). If one assumes no interaction between vacancies, one would predict from a single V_O of 0.73 eV that there would be an estimated energy

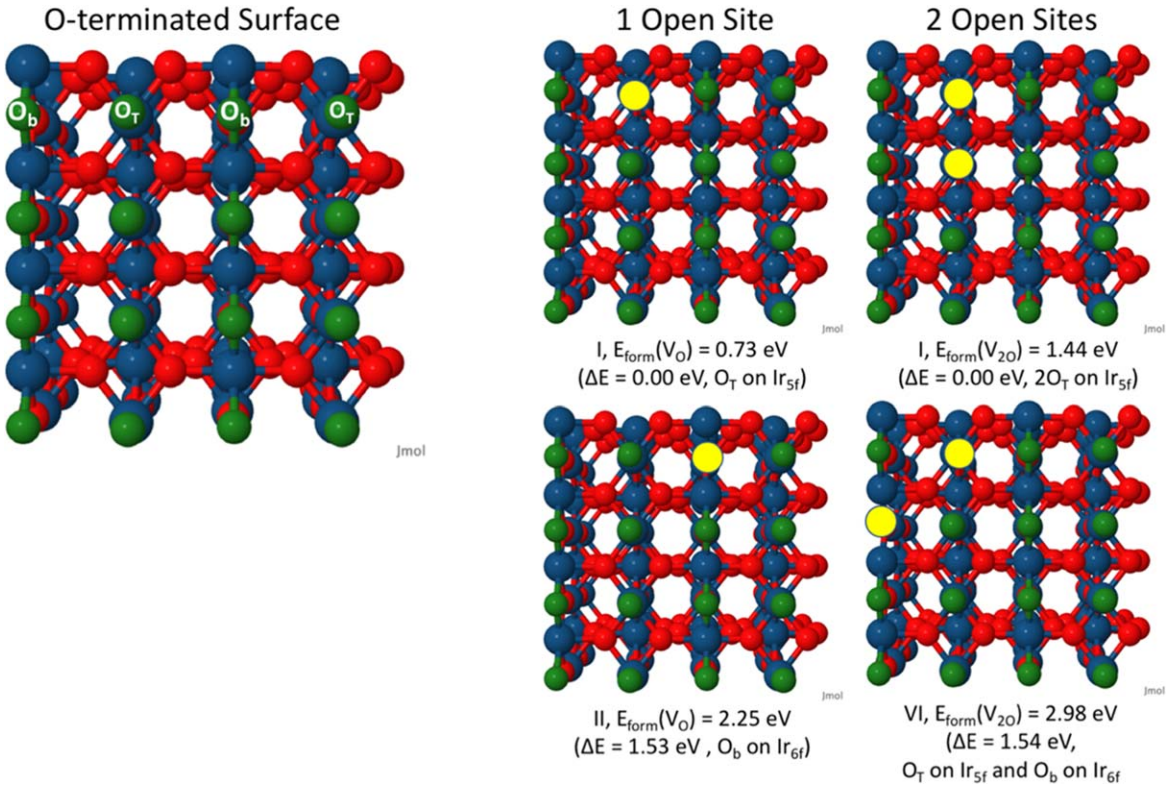

Figure 4. Visualization of the o-terminated surface (**LEFT**) and open sites (V_O, V_{2O}) removed from the surface and their formation energies (**RIGHT**). All 13 unique configurations found for V_{2O} are displayed in SI Fig. 14. All surface oxygens are colored green for visual contrast; bridging (O_b) vs (O_T) surface terminating oxygens are labeled appropriately; open sites used in our analysis are shown colored in yellow.

penalty of 1.46 eV for V_{2O}. However, we note that there is a slight stabilization to removing two *neighboring* oxygens on Ir_{5f} of 0.02 eV.

Indeed, in our search for permutations of two open sites, we found that neighboring open sites often require the lowest formation energy: 1.44 eV for two terminating oxygens, 2.98 eV for one terminating oxygen and one bridging oxygen, and 4.44 for two bridging oxygens. In Setvin et al.'s scanning tunneling microscopy study on vacancies in anatase, they reported that vacancies can aggregate, forming clusters of vacancies depending on temperature and applied current.[67] Specifically, at a little over 300 K, they noted the formation of C2 (two vacancies) and C3 (three vacancies) clusters. Thus, at the typical operating temperature and high overpotentials required for OER, it may be possible that as O_2 desorbs from the surface, open sites are generated on either an O_T site or even on neighboring O_T sites. The extent to which the predicted stabilization survives an applied potential and interaction with an electrolyte would be an interesting question for future work.

We evaluated the key reaction intermediates found for the co-adsorption and OOH* pathways in the context of the oxygen-terminated surface with vacancies for the adsorbates. In Fig. 5, we identify the intermediates and their relative energies (ΔE). The global minimum for the structures requiring 1 metal site (1 M) vs 2 metal sites (2 M) are indicated by "ΔE = 0.00" and surrounding terminating oxygens are labeled as (O_T). Additional 2 M isomers are visualized in SI Fig. 15 and full reaction coordinates are displayed in SI Figs. 16–20.

In Fig. 5, the isomers are classified with a subscript for 1 M or 2 M; the structures requiring 1 M are a different stoichiometry than 2 M. Since the formation of one open site requires the least energy, we utilized this as our reference energy for calculating the adsorption energy: $E_{adsorbate} = E_{surf+ads} - E_{surf,1O} - E_{gas,ads}$. For intermediates utilizing 2 M sites, this pathway only requires the adsorption of OH* in order to initiate the co-adsorption pathway. Therefore, we display the adsorption energy of OH* ($E_{OH} = -3.20$ eV) for the global minimum structure for the 2 M classification. In Fig. 5, we display the adsorption energy of the global minimum structure of $E_{adsorbate}$ for OH* or OOH* adsorbing on an oxygen-terminated surface with one open site. The energy of higher-lying isomers is given as the *difference,* $\Delta E_{adsorbate}$, from the lowest isomer energy.

However, if we consider the case of two open sites on the surface and adsorption of OOH*, then the equation for 2 M structures becomes: $E_{OOH\ on\ 2O} = E_{surf+OOH} - E_{surf,2O} - E_{gas,\ OOH}$. The adsorption energy for isomer I, 2 M is $E_{OOH\ on\ 2O} = -3.13$ eV. With either one open site or two open sites, the co-adsorbed species feature favorable binding of circa −3 eV compared to the OOH remaining intact. In contrast, the adsorption of the OO*/OOH* moieties in the OOH* pathway is not as favorable. For OOH* forming on one open site, the adsorption energy is −2.20 eV. In the following paragraphs, we discuss the bonding motifs that stabilize or destabilize these intermediates.

For the co-adsorption pathway, hydrogen-bonding dominates with the different intermediates in the OH* step and from co-adsorbed O/OH* of the stoichiometric surface now relaxing to isomers I (hydrogen-bonded to O_T) and isomers II (hydrogen-bonded to O_b) on the oxygen-terminated surface. Hydrogen-bonding to an under-coordinated oxygen such as O_T results in greater stabilization than to a bridging oxygen, which already has 2 Ir–O bonds. On the oxygen-terminated surface, surface iridium atoms are no longer under-coordinated, with the O_T "completing" the octahedral coordination geometry of every Ir_{5f} atom. Thus, isomers I-III are relatively close in energy (<0.15 eV from each other) since they retain the completed octahedral coordination geometry of every surface Ir, differing only in the placement of a hydrogen. The deprotonation of isomer I requires a rotation to become isomer II (E_A of 0.09 eV); then to break the O-H bond for hydrogen to hop onto the bridging oxygen (E_A of 0.28 eV), totaling an activation energy of 0.37 eV. We detail the reaction coordinates for the deprotonation steps of I → II → III and II → III in SI Figs. 16–17.

Following deprotonation, the formation of the OO* bridging complex requires an activation energy of 0.48 eV in contrast to only

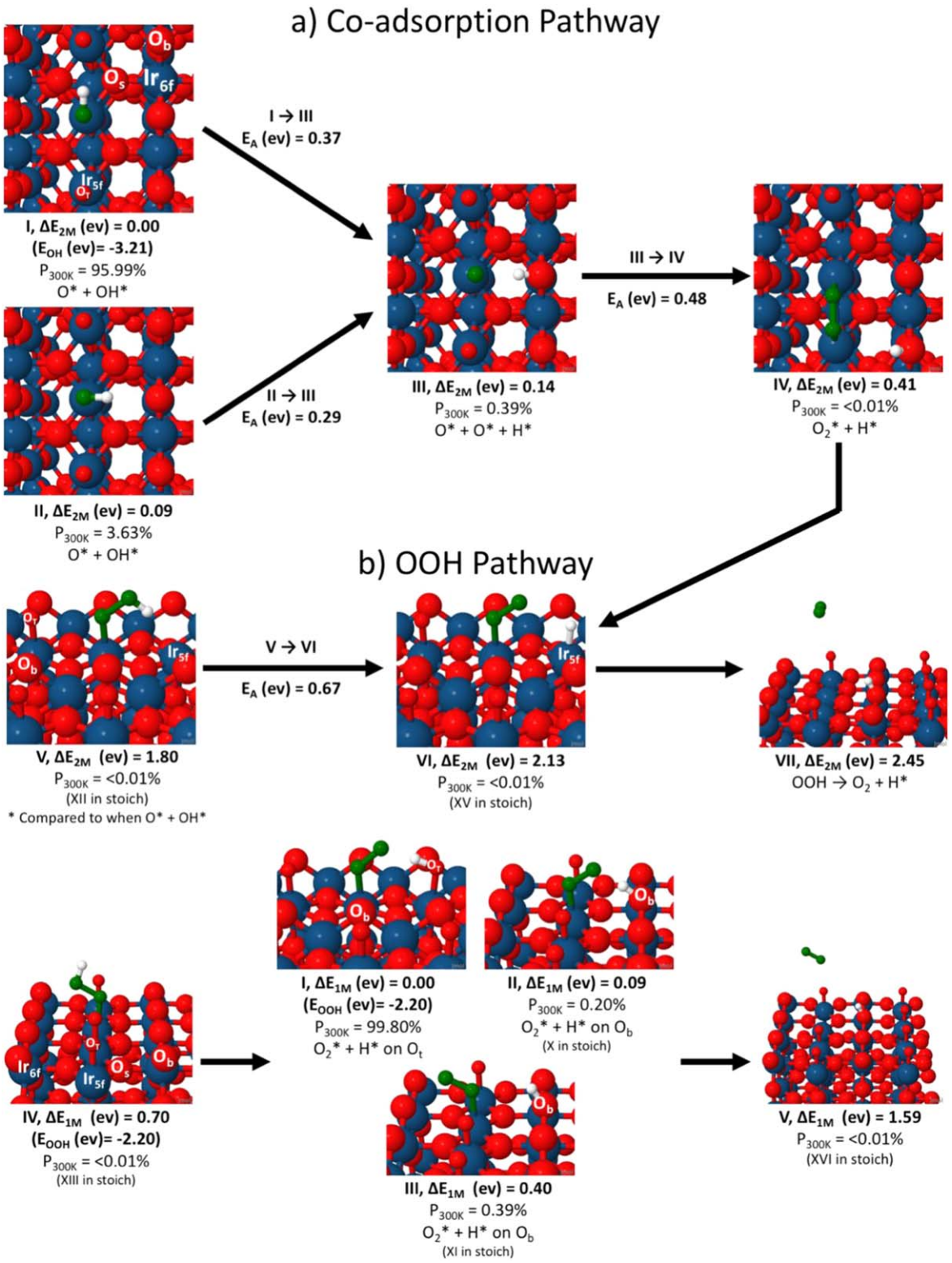

Figure 5. (a) The **co-adsorption pathway** on an oxygen-terminated surface is detailed with relevant isomers that would contribute to the pathway of **O* + OH* → O* + O* + H* → O_2* + H***. (b) The **OOH pathway** on an oxygen-terminated surface is detailed with relevant isomers that would contribute to the pathway of **OOH* → O_2* + H* → O_2 (desorbed) + H***. All isomers are displayed with the energy (ΔE) relative to the global minimum ($\Delta E_{OOH} = 0.00$, denotes global minimum). The adsorption energies E_{OH} and E_{OOH} are in reference to OH* and OOH* adsorbed to one open site on the otherwise oxygen-terminated surface. Boltzmann populations at the room temperature of 300 K are listed underneath the isomer. * refers to an adsorbed species. In order to differentiate the surface atoms on the oxygen-terminated surface, we have included labels (O_T, terminating oxygen; O_b, bridging oxygen; Ir_{5f}, surface 5-fold coordinated iridium atom; Ir_{6f}, surface 6-fold coordinated iridium atom, O_s, surface oxygen). Oxygen atoms in green denote the key reaction intermediates of interest (OH* → O* + H*, OO*, OOH*). In the Supporting Information, we summarize all the isomers in SI Fig. 15 and the full reaction coordinates are visualized in SI Figs. 16–20. Activation energy (E_A) denotates transition state calculations utilizing the cNEB method.

0.34 eV on the stoichiometric surface. The stabilization of isomer III, which retains the octahedral coordination geometry of all surface Ir atoms, therefore results in a higher activation energy for forming the OO* bridging complex. Since this pathway may be sensitive to the placement of the hydrogen, we also calculated the activation energy for forming the OO* bridging complex on a clean oxygen-terminated surface: the change to the barrier is negligible, with the activation energy slightly reduced to 0.46 eV (see SI Fig, 19 for full reaction coordinate). Moreover, we hypothesized that the bridging OO* complex could convert to an OO* complex similar to isomer VI (an intermediate utilizing two metal sites, see Fig. 5b). In the absence of hydrogens on the surface, this OO* complex with only one Ir–O bond is 0.79 eV higher in energy than the bridging OO* complex (see SI Fig. 19). OO*/OOH* intermediates from the OOH* pathway are sensitive to hydrogen placement, this OO* configuration with a hydrogen on the neighboring Ir is ∼2 eV higher in energy than the global minimum (see Figs. 2b, 7b). Likewise, the system with desorbed OO* with a hydrogen on the Ir is a higher energy isomer (ΔE_{2M} = 3.23 eV, visualized in SI Fig. 15) than hydrogen adsorbed on a bridging O (ΔE_{2M} = 2.45 eV).

Thus, considering a possible pathway between isomers IV (ΔE_{2M} = 0.41 eV) → VI (ΔE_{2M} = 2.13 eV) → VII (ΔE_{2M} = 2.45 eV), it becomes apparent that there may be a high energy input required for breaking the first Ir–O bond, but breaking the second Ir–O bond and desorbing O_2 is a state only 0.32 eV higher in energy (VI → VII). We note that the bridging OO* complex of isomer IV also features slightly longer and more distorted Ir–O bonds: the bridging OO* complex features less favorable interactions between the Ir's $5d_{z2\text{-}r2}$ and O's $2p_z$ orbitals compared to either a terminating oxygen or isomer V's OOH* (SI Fig. 21).

For both the terminating oxygen and oxygen from an OOH* species, we observe intense peaks in the PDOS of the O's $2p_z$ orbitals and Ir's $5d_{z2\text{-}r2}$, often reaching ∼1 electron eV^{-1} in height: this occurs at circa −4 eV from the Fermi level for the terminating oxygen and deeper, circa −8 eV, for the OOH* species. In contrast, the bridging OO* complex's orbital overlap to Ir's $5d_{z2\text{-}r2}$ is diffuse with the peaks hovering between circa −0.2 to −0.5 electrons eV^{-1} across the valence band. Intense peaks with optimal overlap are often correlated with the formation of strong bonds, both through the intense "resonance" or overlap between orbitals and donor-acceptor relations, the decrease in one orbital peak and the increase in the another orbital peak signifying shift in the electronic species from one species to another.[47] We note that the resonance between the Ir–O bond for the OO* bridging complex is secondary to that of the two oxygens, where the resonance or overlap between the $2p_z$ orbitals is nearly perfect (SI Fig. 21b). This PDOS discussion corresponds well to the bonding distance between Ir–O: the Ir–O bond for a terminating oxygen is 1.8 Å (the most intense peaks circa −0.8 to −1.0 electrons eV^{-1}); for isomer V's OOH* (intense peaks circa −0.6 to −0.8 electrons eV^{-1}), 1.9 Å; for isomer IV's bridging OO*, 2.0 Å and angled 66° (moderate peaks circa −0.4 to −0.5 electrons eV^{-1}). The presence of the high operating potential of ∼2 V and the dynamics of an electrolyte may potentially exploit the distorted Ir–O bonds of the OO* bridging complex, aiding in desorption of O_2.

For the OOH* pathway, we differentiated key reaction intermediates into ones that utilized one metal site (1 M) or two metal sites (2 M). The pathway utilizing one metal site is typically studied; however, the pathway utilizing two metal sites introduces the co-adsorption pathway or exploits the reactivity of surface Ir atoms to deprotonate an OOH* moiety and the calculations presented here show substantially lower energy associated with this path. Similar to the observations of Gauthier et al. in their solvation study of the OOH* pathway, OOH* often spontaneously dissociates into OO* and H* (hydrogen adsorbing onto the nearby terminating oxygen or bridging oxygen), necessitating addition of a constraining force to keep the OOH* intact.[9] Our results show that the hydrogen prefers to adsorb to the under-coordinated terminating oxygen (hydrogen-bond of ∼1.6 Å); adsorbing to the bridging oxygen results in an isomer 0.09 eV higher in energy (hydrogen-bond of ∼1.5 Å). The OOH* moiety typically studied, isomer XIII on the stoichiometric surface and isomer IV on the O-terminated surface, remains a higher energy isomer of ∼0.6 eV above the deprotonated OO* with H* on a bridging oxygen. Since deprotonation of this OOH* complex is spontaneous on both the stoichiometric and O-terminated surface, only the cNEB barrier for the stable OOH* complex (isomer V-2M) utilizing two metal sites is calculated. On the O-terminated surface, the activation energy is lowered to 0.67 eV compared to the stoichiometric surface, 0.76 eV. For this pathway, the oxygen-terminated surface is more advantageous due to the lowered barrier.

Previous papers have focused on smaller surfaces, specifically, the (1 × 2)[8,9,55] and it is worth asking to what extent surface size has on the results. Hence, we have recalculated the key minima displayed in Fig. 5 on smaller surfaces, (1 × 2) and (2 × 2), and their order and relative energies are listed in Tables IV and V; reaction coordinates may be found in SI Fig. 22. The ordering of the minima remains the same, independent of the size of the supercell. Due to the smaller cell size, the periodic boundary conditions of a smaller surface result in a higher concentration of occupied sites: this, unsurprisingly, leads to slightly less-stable minima relative to the global minimum, e.g. relative energies with respect to isomer I on each surface. Activation energies for formation of the bridging complex were also calculated: the results are relatively consistent across the different-sized oxygen-terminated surfaces, ranging from 0.45–0.49 eV. Differences in the activation energy may arise from the hydrogen relaxing to a slightly different position due to interactions across the periodic images. In particular, isomer V is sensitive to surface size, often spontaneously dissociating into co-adsorbed O* and OH* on the smaller (1 × 2) and (2 × 2) surfaces. A rigorous search for energy minima on these smaller surfaces may be

Table IV. Relative energies of 2M-minima on O-terminated surface, ranging from (1 × 2), (2 × 2), to (4 × 2).

(1 × 2)		(2 × 2)		(2 × 4)	
Isomer	ΔE (eV)	*Isomer*	ΔE (eV)	*Isomer*	ΔE (eV)
I	0.00	I	0.00	I	0.00
II	0.10	II	0.11	II	0.09
III	0.21	III	0.20	III	0.14
IV	0.56	IV	0.47	IV	0.41
V-O_s[a)]	1.66	V–O_s[a)]	1.69	V	1.80
VI	2.08	VI	2.05	VI	2.13
E_A (III → IV)	0.49	E_A (III → IV)	0.45	E_A (III → IV)	0.48
				E_A (O* + O* → OO*)[b)]	0.46

a) Isomer V on a (1 × 2) and (2 × 2) surface often relaxes to isomer I. The topmost O* and H* of this OOH* moiety were fixed in the *z*-axis in order to stabilize this isomer and determine an energy. This isomer OOH* now coordinates the hydrogen to a surface oxygen, O_s, instead of a surface Ir atom.
b) Formation of the OO* bridging complex in the absence of hydrogens was also calculated. See SI Fig. 19 for visualization.

Table V. Relative energies of 1M-minima on O-terminated surface, ranging from (1 × 2), (2 × 2), to (4 × 2).

(1 × 2)		(2 × 2)		(2 × 4)	
Isomer	ΔE (eV)	*Isomer*	ΔE (eV)	*Isomer*	ΔE (eV)
I	0.00	I	0.00	I	0.00
II	0.28	II	0.26	II	0.09
III	0.66	III	0.54	III	0.40
IV	0.83	IV	0.78	IV	0.70
V	1.86	V	2.23	V	1.59

problematic due to interactions across periodic images: on both the (1 × 2) and (2 × 2) surfaces, key reaction intermediates are often <5 Å from each other. This may be related to higher relative energies of the 1 M OO* and OOH* moieties on the oxygen-terminated surface: OO* and OOH* are larger molecules and may be more sensitive to periodic boundary conditions. For these smaller surfaces, the high concentration of sites occupied by larger molecules may result in interactions across the periodic images.

On the oxygen-terminated surface, we highlight that desorption for isomer II → isomer V resulted in a potential energy surface that flattened to a barrier of 1.5 eV once the Ir–O bond distance reached >3.5 Å (SI Fig. 23). This is also the difference in energy between isomer II and V. We expect that this trend occurs on the other surfaces of (1 × 2) and (2 × 2). Ping et al. and Wang et al. focused on a concerted reaction of O_2 desorption followed by H_2O adsorption on their respective oxides of iridium oxide and cobalt oxide: this may lead to a lower barrier than the mechanism utilized here.[55,65] Notably, Ping et al. found the barrier to lower to circa 1 eV for water displacing O_2. Depending on additional considerations e.g. solvation; zero point energies; rotational, vibrational, and translational contributions with respect to gaseous O_2 or 1 M O_2 in liquid water, then they found the barrier to lower to 0.39 eV (gaseous O_2) or 0.56 eV (1 M O_2 in liquid water) at U = 1.53 eV vs NHE, respectively. It is well-known, however, that DFT does result in an "over-binding" error of the O–O bond: Gauthier et al. estimated that the over-binding of O_2 resulted in an error of −0.7 eV relative to the other reference molecules, H_2O and H_2.[9] Thus, the O_2 desorption step may be considerably lower than the 1.0–1.5 eV calculated by the theoretical studies of Ping et al., Wang et al., and in this paper.[55,65]

It suggests that in the complex environment of electrochemistry, the barrier can fall considerably due to the presence of the electrolyte and potential gradient: this will be the topic of a future study. In Gauthier et al.'s study of explicit solvation around OER intermediates, they noted that they found that 12 waters could stabilize the OH* intermediate to ∼0.3 eV; this effect could increase to ∼0.5 eV for OOH*.[9] In his study, 12 waters were arranged upon a (1 × 2) surface; an analogous study on our (2 × 4) surface in combination with the numerous isomers found in this study will require substantial additional sampling and computation. We note that Gauthier et al. applied an electric field of 0.2 V $Å^{-1}$ to their solvated intermediates and found that the change in the energies and geometries to be negligible. Probing the effects of explicit solvent and the electric field on our numerous isomers, however, is of considerable interest and will be the focus of our work in the future. It is our expectation that the introduction of explicit waters would stabilize both the co-adsorbed O* + OH* isomers and OOH* isomers: the degree of added stability might vary, as Gauthier et al. estimated, between 0.3–0.5 eV depending on the hydrogen-bonding network present.[9]

Conclusions

This study highlights the necessity of a larger surface in order to more fully explore mechanistic pathways on a metal oxide surface. Many of the pathways found on the stoichiometric IrO_2 surface are atypical to the current literature on the mechanism of the oxygen evolution reaction but may contribute to the high reactivity of iridium oxide. Indeed, the rutile phase with the thermodynamically stable (110) facet is generally considered less active than other facets due to the low density of under-coordinated surface metal sites compared to iridium oxide's other facets such as (001).[28,68] However, the results above suggest that the (110) facet can be active at both extremes of the surface: the stoichiometric surface with all metal sites available and the largely oxygen-terminated surface with surrounding metal sites populated by oxygen. For the two rate determining steps of the oxygen evolution reaction considered here, the deprotonation of OH* and O_2 evolution via the co-adsorption or OOH* pathway, we observe transition state barriers of <0.7 eV. The initial state of an intermediate can determine the activation barrier: depending on the initial isomer, the deprotonation of OH* features a barrier as low as ∼0.2 eV, albeit with a higher-energy starting point required to access this low-barrier path. In particular, this brings into prominence the possibility of an alternative pathway such as the co-adsorption pathway, which requires multiple intermediate steps of barriers <0.5 eV, to form a bridging OO* complex.

Moreover, the mechanistic pathways detailed here for IrO_2 (110) offers insight into possible understanding and improvement of OER catalyst design. Namely, OER may occur through multiple, intermediate steps beyond the typical 4-step, proton-electron pathway. Rather than tuning catalysts for the formation of an OOH* species, OER catalysts may be optimized to engage co-adsorbed species of O*/OH* and consequently form a bridging O_2* complex. The OOH* pathway is predicated on both an adsorbed O* and water-splitting to form an OOH* intermediate; in contrast, the co-adsorption pathway may utilize terminating oxide and hydroxide species formed through experimental passivation or potential cycling. More nuanced prediction of the OER mechanism may be required for the development and optimization of reduced and non-Platinum Group Metal catalysts: our detailing of different isomers at each step of the OER allows us to identify various rate-determining steps. In particular, we showcase that the various surface species of a metal oxide can engage in catalysis: notably, Ir can deprotonate an OOH* species; nearest-neighbor Ir atoms can also help form O_2*. Other metal oxides, modified through straining the lattice, doping, exposing specific facets, or incorporating defects, may also exploit these pathways and, hopefully, reduce the overpotentials necessary for OER and act as an alternative to Ir-based catalysts.

Whether the co-adsorption pathway identified here is possible or relevant in practice will depend on operating conditions. The novelty of the pathway may be a concern but the strong energetic driving force for OOH* dissociation found in all of our calculations argues that it should be considered for future work. We note that mapping this number of intermediates and reaction pathways is computationally intensive, but we believe it will be of considerable interest to the catalysis community to incorporate this possibility into more realistic conditions that include solvation and the potential gradient. This will be the topic of a future study. In addition, the suggestion that alternative reaction intermediates could be involved may suggest experiments to identify intermediates during OER so as to better understand the relationship of our idealized calculations to how the catalyst may behave under operating conditions. For instance, recent experimental studies in vibrational and in situ ambient X-ray photoelectron spectroscopy have been able to detect changes in surface species to a high degree of sensitivity[10,18,69] and similar experiments may help in confirming or ruling out the co-adsorption path for specific conditions.

Acknowledgments

This work was authored by the National Renewable Energy Laboratory (NREL), operated by Alliance for Sustainable Energy, LLC, for the U.S. Department of Energy (DOE) under Contract No. DE-AC36-08GO28308. This work was partly supported by the Laboratory Directed Research and Development (LDRD) Program

at NREL through a Director's Fellowship for M. Ha and partly with support from the HydroGEN Advanced Water Splitting Materials Consortium, established as part of the Energy Materials Network under the U.S. Department of Energy, Office of Energy Efficiency and Renewable Energy, Hydrogen and Fuel Cell Technologies Office. LDRD funding supported calculations of surface-induced dissociation and reaction intermediate adsorption energies. HydroGEN funding supported the calculation of reaction barriers and the examination of mechanistic pathways on the oxygen terminated surface. We thank Tadashi Ogitsu and Adam Weber for discussions that led us to re-evaluate the mechanistic pathways found on the stoichiometric surface and map them onto the oxygen-terminated surface. The views expressed in the article do not necessarily represent the views of the DOE or the U.S. Government. The U.S. Government retains and the publisher, by accepting the article for publication, acknowledges that the U.S. Government retains a nonexclusive, paid-up, irrevocable, worldwide license to publish or reproduce the published form of this work, or allow others to do so, for U.S. Government purposes.

ORCID

Mai-Anh Ha https://orcid.org/0000-0002-9137-2621
Ross E. Larsen https://orcid.org/0000-0002-2928-9835

References

1. B. Pivovar, N. Rustagi, and S. Satyapal, "Hydrogen at scale (H2@ Scale): key to a clean, economic, and sustainable energy system." *Electrochem. Soc. Interf.*, **27**, 47 (2018).
2. P. Chiesa, G. Lozza, and L. Mazzocchi, "Using hydrogen as gas turbine fuel." *J. Eng. Gas Turbines Power*, **127**, 73 (2005).
3. D. M. Todd and R. A. Battista, *Proceedings of the IChemE "Gasification 4 of the Future" Conference*, Noordwijk, the Netherlands, April 11–13, 2000 (2000), Demonstrated applicability of hydrogen fuel for gas turbines.
4. A. P. Simpson and A. E. Lutz, "Exergy analysis of hydrogen production via steam methane reforming." *Int. J. Hydrogen Energy*, **32**, 4811 (2007).
5. Fuel Cell Technologies Office, *Multi-Year Research, Development, and Demonstration Plan: section 3.1 Hydrogen Production.*, Department of Energy, 1 (2015), https://www.energy.gov/eere/fuelcells/downloads/hydrogen-and-fuel-cell-technologies-office-multi-year-research-development.
6. A. Manabe, M. Kashiwase, T. Hashimoto, T. Hayashida, A. Kato, K. Hirao, I. Shimomura, and I. Nagashima, "Basic study of alkaline water electrolysis." *Electrochim. Acta*, **100**, 249 (2013).
7. S. M. Alia and G. C. Anderson, "Iridium oxygen evolution activity and durability baselines in rotating disk electrode half-cells." *J. Electrochem. Soc.*, **166**, F282 (2019).
8. I. C. Man, H. Y. Su, F. Calle-Vallejo, H. A. Hansen, J. I. Martínez, N. G. Inoglu, J. Kitchin, T. F. Jaramillo, J. K. Nørskov, and J. Rossmeisl, "universality in oxygen evolution electrocatalysis on oxide surfaces." *ChemCatChem*, **3**, 1159 (2011).
9. J. A. Gauthier, C. F. Dickens, L. D. Chen, A. D. Doyle, and J. K. Nørskov, "Solvation effects for oxygen evolution reaction catalysis on IrO2 (110)." *J. Phys. Chem. C*, **121**, 11455 (2017).
10. H. G. Sanchez Casalongue, M. L. Ng, S. Kaya, D. Friebel, H. Ogasawara, and A. Nilsson, "*In situ* observation of surface species on iridium oxide nanoparticles during the oxygen evolution reaction." *Angew. Chem. Int. Ed.*, **53**, 7169 (2014).
11. N. Danilovic, R. Subbaraman, K.-C. Chang, S. H. Chang, Y. J. Kang, J. Snyder, A. P. Paulikas, D. Strmcnik, Y.-T. Kim, and D. Myers, "Activity–stability trends for the oxygen evolution reaction on monometallic oxides in acidic environments." *J. Phys. Chem. Lett.*, **5**, 2474 (2014).
12. T. Reier, M. Oezaslan, and P. Strasser, "Electrocatalytic oxygen evolution reaction (OER) on Ru, Ir, and Pt catalysts: a comparative study of nanoparticles and bulk materials." *ACS Cat.*, **2**, 1765 (2012).
13. A. Minguzzi, C. Locatelli, O. Lugaresi, E. Achilli, G. Cappelletti, M. Scavini, M. Coduri, P. Masala, B. Sacchi, and A. Vertova, "Easy accommodation of different oxidation states in iridium oxide nanoparticles with different hydration degree as water oxidation electrocatalysts." *ACS Cat.*, **5**, 5104 (2015).
14. V. Pfeifer, T. E. Jones, J. J. V. Vélez, R. Arrigo, S. Piccinin, M. Hävecker, A. Knop-Gericke, and R. Schlögl, "*In situ* observation of reactive oxygen species forming on oxygen-evolving iridium surfaces." *Chem. Sci.*, **8**, 2143 (2017).
15. S. M. Alia, M.-A. Ha, G. C. Anderson, C. Ngo, S. Pylypenko, and R. E. Larsen, "The roles of oxide growth and sub-surface facets in oxygen evolution activity of iridium and its impact on electrolysis." *J. Electrochem. Soc.*, **166**, F1243 (2019).
16. S. M. Alia, S. Shulda, C. Ngo, S. Pylypenko, and B. S. Pivovar, "Iridium-based nanowires as highly active, Oxygen evolution reaction electrocatalysts." *ACS Cat.*, **8**, 2111 (2018).
17. F. Godínez-Salomón, L. Albiter, S. M. Alia, B. S. Pivovar, L. E. Camacho-Forero, P. B. Balbuena, R. Mendoza-Cruz, M. J. Arellano-Jimenez, and C. P. Rhodes, "Self-supported hydrous iridium–nickel oxide two-dimensional nanoframes for high activity oxygen evolution electrocatalysts." *ACS Cat.*, **8**, 10498 (2018).
18. Z. Pavlovic, C. Ranjan, Q. Gao, M. van Gastel, and R. Schlögl, "Probing the structure of a water-Oxidizing anodic iridium oxide catalyst using raman spectroscopy." *ACS Cat.*, **6**, 8098 (2016).
19. D. R. Baker, M. B. Graziano, and B. M. Hanrahan, "Nanostructured antireflective iridium oxide coating for water oxidation." *J. Phys. Chem. C*, **122**, 12207 (2018).
20. S. Marini, P. Salvi, P. Nelli, R. Pesenti, M. Villa, M. Berrettoni, G. Zangari, and Y. Kiros, "Advanced alkaline water electrolysis." *Electrochim. Acta*, **82**, 384 (2012).
21. T. H. Yu, T. Hofmann, Y. Sha, B. V. Merinov, D. J. Myers, C. Heske, and W. A. Goddard III, "Finding correlations of the oxygen reduction reaction activity of transition metal catalysts with parameters obtained from quantum mechanics." *J. Phys. Chem. C*, **117**, 26598 (2013).
22. M.-A. Ha, E. T. Baxter, A. C. Cass, S. L. Anderson, and A. N. Alexandrova, "Boron switch for selectivity of catalytic dehydrogenation on size-selected Pt clusters on Al_2O_3." *J. Am. Chem. Soc.*, **139**, 11568 (2017).
23. E. T. Baxter, M.-A. Ha, A. C. Cass, A. N. Alexandrova, and S. L. Anderson, "Ethylene dehydrogenation on Pt4, 7, 8 Clusters on Al_2O_3: Strong cluster size dependence linked to preferred catalyst morphologies." *ACS Cat.*, **7**, 3322 (2017).
24. A. Halder, M.-A. Ha, H. Zhai, B. Yang, M. J. Pellin, S. Seifert, A. N. Alexandrova, and S. Vajda, "Oxidative dehydrogenation of cyclohexane by Cu vs Pd clusters: selectivity control by specific cluster dynamics." *ChemCatChem*, **12**, 1307 (2020).
25. S. M. Alia, C. Ngo, S. Shulda, M.-A. Ha, A. A. Dameron, J. N. Weker, K. C. Neyerlin, S. S. Kocha, S. Pylypenko, and B. S. Pivovar, "Exceptional oxygen reduction reaction activity and durability of platinum–nickel nanowires through synthesis and post-treatment optimization." *ACS Omega*, **2**, 1408 (2017).
26. J. A. Rodriguez, P. Liu, D. J. Stacchiola, S. D. Senanayake, M. G. White, and J. G. Chen, "Hydrogenation of CO_2 to methanol: importance of metal–oxide and metal–carbide interfaces in the activation of CO_2." *ACS Cat.*, **5**, 6696 (2015).
27. B. von Boehn and R. Imbihl, "Chemical wave patterns and oxide redistribution during methanol oxidation on a V-oxide promoted Rh (110) surface." *J. Phys. Chem. C*, **122**, 12694 (2018).
28. O. Matz and M. Calatayud, "Periodic DFT study of rutile IrO2: surface reactivity and catechol adsorption." *J. Phys. Chem. C*, **121**, 13135 (2017).
29. J. Rossmeisl, Z.-W. Qu, H. Zhu, G.-J. Kroes, and J. K. Nørskov, "Electrolysis of water on oxide surfaces." *J. Electroanal. Chem.*, **607**, 83 (2007).
30. G. Henkelman, G. Jóhannesson, and H. Jónsson, "Methods for finding saddle points and minimum energy paths.." *Theoretical Methods in Condensed Phase Chemistry* (Springer, Berlin) p. 269 (2002).
31. G. Henkelman, B. P. Uberuaga, and H. Jónsson, "A climbing image nudged elastic band method for finding saddle points and minimum energy paths." *J. Chem. Phys.*, **113**, 9901 (2000).
32. G. Henkelman and H. Jónsson, "Improved tangent estimate in the nudged elastic band method for finding minimum energy paths and saddle points." *J. Chem. Phys.*, **113**, 9978 (2000).
33. G. Henkelman and H. Jónsson, "A dimer method for finding saddle points on high dimensional potential surfaces using only first derivatives." *J. Chem. Phys.*, **111**, 7010 (1999).
34. G. Kresse and J. Hafner, "*Ab initio* molecular dynamics for liquid metals." *Phys. Rev. B*, **47**, 558 (1993).
35. G. Kresse and J. Hafner, "*Ab initio* molecular-dynamics simulation of the liquid-metal–amorphous-semiconductor transition in germanium." *Phys. Rev. B*, **49**, 14251 (1994).
36. G. Kresse and J. Furthmüller, "Efficiency of ab-initio total energy calculations for metals and semiconductors using a plane-wave basis set." *Comput. Mater. Sci.*, **6**, 15 (1996).
37. G. Kresse and J. Furthmüller, "Efficient iterative schemes for *ab initio* total-energy calculations using a plane-wave basis set." *Phys. Rev. B*, **54**, 11169 (1996).
38. P. E. Blöchl, "Projector augmented-wave method." *Phys. Rev. B*, **50**, 17953 (1994).
39. G. Kresse and D. Joubert, "From ultrasoft pseudopotentials to the projector augmented-wave method." *Phys. Rev. B*, **59**, 1758 (1999).
40. J. P. Perdew, A. Ruzsinszky, G. I. Csonka, O. A. Vydrov, G. E. Scuseria, L. A. Constantin, X. Zhou, and K. Burke, "Restoring the density-gradient expansion for exchange in solids and surfaces." *Phys. Rev. Lett.*, **100**, 136406 (2008).
41. J. P. Perdew, K. Burke, and M. Ernzerhof, "Generalized gradient approximation made simple." *Phys. Rev. Lett.*, **77**, 3865 (1996).
42. J. Kahk, C. Poll, F. Oropeza, J. Ablett, D. Céolin, J. Rueff, S. Agrestini, Y. Utsumi, K. Tsuei, and Y. Liao, "Understanding the electronic structure of IrO2 using hard-X-ray photoelectron spectroscopy and density-functional theory." *Phys. Rev. Lett.*, **112**, 117601 (2014).
43. R. W. G. Wyckoff, *Crystal Structures.* (Wiley, New York) (1963).
44. M.-A. Haa and A. N. Alexandrova, "Oxygen vacancies of anatase (101): Extreme sensitivity to the density functional theory method." *J. Chem. Theory Comput.*, **12**, 2889 (2016).
45. D. Sheppard, P. Xiao, W. Chemelewski, D. D. Johnson, and G. Henkelman, "A generalized solid-state nudged elastic band method." *J. Chem. Phys.*, **136**, 074103 (2012).
46. H. Jónsson, G. Mills, and K. W. Jacobsen, "Nudged elastic band method for finding minimum energy paths of transitions." *Classical and quantum dynamics in condensed phase simulations* (World Scientific, Singapore) p. 385 (1998).
47. R. Hoffmann, "A chemical and theoretical way to look at bonding on surfaces." *Rev. Mod. Phys.*, **60**, 601 (1988).
48. M. Yu and D. R. Trinkle, "Accurate and efficient algorithm for Bader charge integration." *J. Chem. Phys.*, **134**, 064111 (2011).

49. W. Tang, E. Sanville, and G. Henkelman, "A grid-based Bader analysis algorithm without lattice bias." *J. Phys. Condens. Matter*, **21**, 084204 (2009).
50. E. Sanville, S. D. Kenny, R. Smith, and G. Henkelman, "Improved grid-based algorithm for Bader charge allocation." *J. Comput. Chem.*, **28**, 899 (2007).
51. G. Henkelman, A. Arnaldsson, and H. Jónsson, "A fast and robust algorithm for Bader decomposition of charge density." *Comput. Mater. Sci.*, **36**, 354 (2006).
52. J. S. Filhol and M. Neurock, "Elucidation of the electrochemical activation of water over Pd by first principles." *Angew. Chem. Int. Ed.*, **45**, 402 (2006).
53. R. Jinnouchi, K. Kodama, and Y. Morimoto, "DFT calculations on H, OH and O adsorbate formations on Pt (111) and Pt (332) electrodes." *J. Electroanal. Chem.*, **716**, 31 (2014).
54. P. J. Lindan, N. Harrison, and M. Gillan, "Mixed dissociative and molecular adsorption of water on the rutile (110) surface." *Phys. Rev. Lett.*, **80**, 762 (1998).
55. Y. Ping, R. J. Nielsen, and W. A. Goddard, "The reaction mechanism with free energy barriers at constant potentials for the oxygen evolution reaction at the IrO2 (110) surface." *J. Am. Chem. Soc.*, **139**, 149 (2017).
56. J. K. Nørskov, J. Rossmeisl, A. Logadottir, L. Lindqvist, J. R. Kitchin, T. Bligaard, and H. Jonsson, "Origin of the overpotential for oxygen reduction at a fuel-cell cathode." *J. Phys. Chem. B*, **108**, 17886 (2004).
57. E. E. Benson, M.-A. Ha, B. A. Gregg, J. van de Lagemaat, N. R. Neale, and D. Svedruzic, "Dynamic tuning of a thin film electrocatalyst by tensile strain." *Sci. Rep.*, **9**, 15906 (2019).
58. N. Agmon, "The grotthuss mechanism." *Chem. Phys. Lett.*, **244**, 456 (1995).
59. J. McIntyre, W. Peck, and S. Nakahara, "Oxidation state changes and structure of electrochromic iridium oxide films." *J. Electrochem. Soc.*, **127**, 1264 (1980).
60. C. J. Calzado, N. C. Hernández, and J. F. Sanz, "Effect of on-site Coulomb repulsion term U on the band-gap states of the reduced rutile (110) TiO_2 surface." *Phys. Rev. B*, **77**, 045118 (2008).
61. P. M. Kowalski, M. F. Camellone, N. N. Nair, B. Meyer, and D. Marx, "Charge localization dynamics induced by oxygen vacancies on the TiO_2 (110) surface." *Phys. Rev. Lett.*, **105**, 146405 (2010).
62. T. Minato, Y. Sainoo, Y. Kim, H. S. Kato, K.-I. Aika, M. Kawai, J. Zhao, H. Petek, T. Huang, and W. He, "The electronic structure of oxygen atom vacancy and hydroxyl impurity defects on titanium dioxide (110) surface." *J. Chem. Phys.*, **130**, 124502 (2009).
63. P. Krüger, S. Bourgeois, B. Domenichini, H. Magnan, D. Chandesris, P. Le Fevre, A. Flank, J. Jupille, L. Floreano, and A. Cossaro, "Defect states at the TiO_2 (110) surface probed by resonant photoelectron diffraction." *Phys. Rev. Lett.*, **100**, 055501 (2008).
64. G. Bronoel and J. Reby, "Mechanism of oxygen evolution in basic medium at a nickel electrode." *Electrochim. Acta*, **25**, 973 (1980).
65. L.-P. Wang and T. Van Voorhis, "Direct-Coupling O2 bond forming a pathway in cobalt oxide water oxidation catalysts." *J. Phys. Chem. Lett.*, **2**, 2200 (2011).
66. Y. Surendranath, M. W. Kanan, and D. G. Nocera, "Mechanistic studies of the oxygen evolution reaction by a cobalt-phosphate catalyst at neutral pH." *J. Am. Chem. Soc.*, **132**, 16501 (2010).
67. M. Setvín, U. Aschauer, P. Scheiber, Y.-F. Li, W. Hou, M. Schmid, A. Selloni, and U. Diebold, "Reaction of O2 with subsurface oxygen vacancies on TiO_2 anatase (101)." *Science*, **341**, 988 (2013).
68. K. A. Stoerzinger, L. Qiao, M. D. Biegalski, and Y. Shao-Horn, "Orientation-dependent oxygen evolution activities of rutile IrO2 and RuO2." *J. Phys. Chem. Lett.*, **5**, 1636 (2014).
69. J. Qian, Y. Ye, H. Yang, J. Yano, E. J. Crumlin, and W. A. Goddard, "Initial steps in forming the electrode–electrolyte interface: H_2O adsorption and complex formation on the Ag(111) surface from combining quantum mechanics calculations and ambient pressure X-ray photoelectron spectroscopy." *J. Am. Chem. Soc.*, **141**, 6946 (2019).